The Astrophysical Journal, 905:101 (13pp), 2020 December 20 https://doi.org/10.3847/1538-4357/abc2cf

Transition Probabilities and Collision Strengths for Fine-structure Levels Excitation of Ti II

S. S. Tayal[1] and O. Zatsarinny[2]
[1] Clark Atlanta University, Atlanta, GA 30314, USA; STayal@cau.edu
[2] Drake University, Des Moines, IA, 50311, USA
Received 2020 July 31; revised 2020 September 10; accepted 2020 September 29; published 2020 December 17

Abstract

Several spectral features from the stellar and nebular objects arise due to the iron-peak Ti II fine-structure excitations. Transition probabilities and electron excitation collision strengths of iron-peak elements are important for a meaningful interpretation and analysis of the observed astrophysical spectra. Accurate description of atomic structure with open $3d$-shell elements is the key to the reliable and accurate computation of radiative and collision rates. The term-dependent one-electron orbitals in the multiconfiguration Hartree–Fock approach with adjustable configuration expansions and semi-empirical fine-tuning for energy corrections have been used in achieving highly accurate target description. A total of 314 Ti II fine-structure levels of the ground $3d^24s$ and excited $3d^3$, $3d4s^2$, $3d^24p$, $3d^25s$, $3d4s4p$, $3d^24d$, $3d^25p$, and $3d^24f$ configurations have been included in the calculations of these atomic parameters. The present calculation of collision strengths has been performed in a close-coupling approximation based on the B-spline Breit–Pauli R-matrix method with inclusion of spin–orbit interaction term in the Hamiltonian matrices. Effective collision strengths over a Maxwellian distribution of electron velocities at temperatures in the range from 10^3 to 10^5 K have been reported for transitions between the 314 fine-structure levels. These wide array of transitions give rise to many main Ti II infrared, optical, and ultraviolet lines from a variety of astrophysical objects. Our calculated parameters are compared with the available other theoretical and experimental results, and through this comparison likely uncertainties in our results have been estimated, especially for transitions among the low-lying fine-structure levels of astrophysical importance.

Unified Astronomy Thesaurus concepts: Laboratory astrophysics (2004); Excitation rates (2067)

Supporting material: machine-readable tables

1. Introduction

The iron-group elements have high abundances in various astronomical objects and cover a wide metallicity range. The abundance patterns with metallicity can assist to understand the stellar nucleosynthesis and galactic chemical enrichment. The combination of infrared and optical lines offer good spectral diagnostics of astrophysical plasmas. In particular, numerous Ti II lines have been detected in the spectrum of the η Carinae, one of the very shining stars of our Galaxy, in a broad wavelength region from ultraviolet to infrared. The Ti II resonance transitions at 191.06 nm and 191.09 nm have been observed in the spectra of large Magellanic Cloud toward *SN*1987*A* and in QSO absorption line systems (Meyer et al. 1995; Prochaska & Wolfe 1999). In the last few decades considerable efforts have been made to generate various atomic data sets for iron-peak elements. However, Ti II radiative and collision rates data are relatively scarce in comparison to other iron-peak elements. The Ti II forbidden lines play an important role in the modeling of low-density astrophysical plasmas. Usually, the forbidden transitions are from metastable states, which decay mostly through electric quadrupole (E2) and magnetic dipole (M1) transitions. The first experimental lifetime investigation of metastable levels in Ti II was carried out by Hartman et al. (2003) as a part of the FERRUM Project. They measured the lifetime of the $3d^2(^3P)4s^4P_{5/2}$ level using the laser probing technique and obtained a very long lifetime of $28 \pm 10s$. This value, however, is more than a factor of 2 larger than their own theoretical calculation. Later, Hartman et al. (2005) reported lifetimes of four more levels, $3d^2(^3P)4s^4P_{3/2}$, $3d^2(^3P)4s^2P_{1/2}$, and $3d4s^{22}D_{3/2,5/2}$, together with measurement of decay rates from the $3d4s^{22}D_{3/2,5/2}$ levels. There were large uncertainties associated with these measurements as the lifetimes were not corrected for the effect of repopulation. The collision de-excitation leads to quenching, which eventually results in the shorter lifetimes than measured from pure radiative transitions. Royen et al. (2007) developed a method of extracting radiative decay lifetimes of the long-lived metastable levels by correcting for the systematic effect of repopulation. This technique has been used by Palmeri et al. (2008) to obtain lifetimes of two additional levels, $3d^{32}D_{5/2}$ and $3d^2(^3P)4s^2P_{3/2}$, along with revised values of the previously published lifetimes. Palmeri et al. (2008) also calculated lifetimes of 13 metastable levels using the Cowan code (Cowan 1981) based on a pseudo-relativistic Hartree–Fock model with empirically adjusted radial integral values, and compared their calculated results with measurements. They also presented transition probabilities for several decay channels from these metastable levels.

The first extensive calculation of transition probabilities for the forbidden transitions among the Ti II lowest 37 even parity levels of $3d^24s$, $3d^3$, and $3d4s^2$ configurations has been presented by Deb et al. (2009). They used the atomic structure code CIV3 of Hibbert (1975) and Hibbert et al. (1991). The Breit–Pauli interactions in the Hamiltonian matrices have been considered to account for the relativistic effects. Deb et al. (2009) also employed a fine-tuning technique (Hibbert 1996), that allowed them to adjust calculated excited levels energies to the observed values. Agreement between the calculated and observed lifetimes of some metastable states has been found to be good, and the agreement with calculated values of Palmeri et al. (2008) has been between 5% and 50% for the 29 Ti II

lines observed in the η Carinae Sr-filament. Deb et al. (2009) presented transition probabilities for 535 forbidden transitions. Deb et al. (2009) also concluded that both valence–valence and core–valence correlation effects due to single and double promotions are important for these forbidden transitions.

The $3d^24p$ and $3d4s4p$ configurations in Ti II represent the lowest odd parity configurations. The electric allowed (E1) transitions between these configurations and the lower even parity metastable levels give rise to strong spectral lines in Ti II. Several experimental and theoretical studies have been carried out for the allowed E1 transitions. The oscillator strengths for the Ti II resonance lines at 191.06 nm and 191.09 nm have been measured by Wiese et al. (2001). The review of earlier measurements is presented in a recent publication of Lundberg et al. (2016). They also reported new experimental radiative lifetimes of four $4p$ levels and six $5s$ levels of Ti II. They determined absolute transition probabilities and log gf values for 57 transitions by combining their measured lifetimes for the five $5s$ levels with the experimental branching fractions of Pickering et al. (2001). Lundberg et al. also calculated transition probabilities for 3336 spectral lines in the wavelength range from 138 to 9966 nm using the pseudo-relativistic Hartree–Fock method (Cowan 1981) with inclusion of core-polarization effects. Their online Table 7 contains an extensive collection of radiative transition rates together with the all other available radiative rates for Ti II spectral lines. All theoretical studies of oscillator strengths for E1 transitions in Ti II have been carried out in semi-empirical approximations. The most recent and extensive of these studies are the calculation of Kurucz (2011) using the Cowan code (Cowan 1981) and the calculation of Ruczkowski et al. (2016) using a pseudo-relativistic Hartree–Fock model with empirically adjusted radial integral values. These data cover a wide range of transitions and lifetimes for the 45 odd parity and 30 even parity Ti II levels belonging to the $3d^24p$, $3d^24d$, and $3d^25s$ configurations.

In contrast to radiative data, there is a lack of electron-impact excitation collision rates for Ti II in the literature. The electron-impact excitation collision strengths of Ti II have been previously calculated by Bautista et al. (2006). They employed the Breit–Pauli R-matrix method (Burke et al. 1994), and included the lowest 82 energy levels of the $3d^3$, $3d^24s$, $3d^24p$, and $3d4s^2$ configurations in the close-coupling expansion. The transitions rates and collision strengths for the forbidden transitions were calculated mostly for use in their modeling calculations. They presented log gf values for some transitions and compared their results with the measured values of Pickering et al. (2001), and Bizzarri et al. (1993), recommended values from the National Institute of Standards and Technology (NIST) compilation, and computed values of Kurucz (2000). The transition rates for the forbidden transitions were used to calculate lifetimes for the five metastable levels and these were compared with the experimental lifetimes from the FERRUM project (Hartman et al. 2003, 2005). The calculated lifetimes were found to agree within 50% of the measured values. They presented collision strengths of six forbidden transitions for excitation from the $3d^2(^3F)4sa^4F_{3/2}$ level to $a^4F_{5/2}$, $a^4F_{7/2}$, $a^4F_{9/2}$, $b^4F_{3/2}$, $a^2F_{7/2}$, $a^2D_{3/2}$ levels at temperatures from 5000 K to 20,000 K graphically.

Our aim in the present work is to perform elaborate and extensive calculations for the electron scattering from Ti II to provide comprehensive data sets of electron excitation collision strengths and effective collision strengths together with radiative transitions probabilities for a wide range of allowed and forbidden transitions in Ti II. Our comprehensive atomic data can be used for a detailed analysis and interpretation of the available measured astrophysical spectra. The present calculations have been carried out in the close-coupling approximation using the B-spline Breit–Pauli R-matrix method. The close-coupling expansion included 314 fine-structure levels of Ti II belonging to terms of the ground $3d^24s$ and excited $3d^3$, $3d4s^2$, $3d^24p$, $3d^25s$, $3d4s4p$, $3d^24d$, $3d^25p$, and $3d^24f$ configurations. The accurate target description of the open $3d$-shell iron-peak elements such as Ti II offers some challenges because individual orbitals in the $3d$ shell with different occupation show strong term dependence. The term dependence of the one-electron orbitals can be accounted for either by adding a number of specially designed pseudo-orbitals to a set of orthogonal one-electron orbitals or by using sets of term-dependent non-orthogonal orbitals. The former approach will require large configuration–interaction (CI) expansions, which may become computationally intractable in the case of open $3d$-shell systems. On the other hand, the term-dependent non-orthogonal orbitals approach requires a large number of non-orthogonal one-electron orbitals, but computationally manageable CI expansions. In this respect, our B-spline R-matrix (BSR) method with the term-dependent non-orthogonal orbitals (Zatsarinny 2006) has the advantage of obtaining a highly accurate target description with manageable CI expansions as was illustrated in our recent calculations for electron collisions with Fe II (Tayal & Zatsarinny 2018) and Cr II (Tayal & Zatsarinny 2020) where the flexibility of the code has been used to generate a very accurate target description.

The relativistic effects have been included in the close-coupling expansions through the Breit–Pauli Hamiltonian. For a more accurate description of the spin–orbit mixing of the various terms, the target non-relativistic (LS) energies have been fine-tuned to represent the observed fine-structure splitting as accurately as possible. This procedure is intended to enhance the accuracy of term-mixing coefficients in the target wave functions and, therefore, to increase the accuracy of forbidden transitions. Our collision rates have been compared with the available calculation of Bautista et al. (2006) to assess the accuracy of our calculated effective collision strengths. We have used the comparison of radiative rates and lifetimes to check the accuracy of the present target description and, therefore to some extent, the accuracy of the associated collision rates as well.

2. Computational Methods

2.1. Description of Target Wave Functions

The target wave functions have been generated by using the multiconfiguration Hartree–Fock (MCHF) code of Froese Fischer et al. (2007) together with the CI code for non-orthogonal orbitals (Zatsarinny & Froese Fisher 2000, 2009) in fully ab initio calculations without any semi-empirical correction. The $1s$, $2s$, $2p$, $3s$, and $3p$ orbitals of the inner core $[1s^22s^22p^63s^23p^6]$ have been determined from a Hartree–Fock calculation for the ground state $3d^24s$, and the same core orbitals have been used for all states considered in the present work. The valence spectroscopic $3d$, $4l$ ($l = 0 - 3$), $5s$, and $5p$ orbitals have been determined in the term-average approximation for each main configuration independently. The valence orbitals have been found to have noticeable term-dependence. For example, the average radius of the $3d$ orbital

was found to be 1.56, 1.69, and 1.27 au for the $3d^2 4s$, $3d^3$, and $3d4s^2$ configurations, respectively, and the term-dependence gave rise to correction in the configuration energies of about 0.1 Ry. It indicates the significance of term dependence of one-electron orbitals in the accurate calculation of term energies. In addition to the spectroscopic orbitals, we also determined several sets of the $5l$ and $6l$ ($l = 0 - 4$) correlation orbitals. The correlation orbitals have been obtained specifically for one chosen term of a given configuration using the MCHF code, and then the set of these correlated orbitals was kept fixed for all terms of that configuration.

Then we considered the one- and two-electron promotions of the inner $3s$ and $3p$ orbitals to the valence orbitals what accounted for the core–valence correlation effects. Both valence–valence and core–valence correlation was found to be important to obtain well-converged atomic wave functions. To keep the target CI expansions to a reasonable size, the final target expansions were restricted to the configurations with mixing coefficients larger than ∼0.02.

The consideration of all possible single and double promotions of valence electrons in Ti II leads to very large configuration expansions. It is basically due to many different intermediate terms of the open $3d$ shell. The large target expansions are not feasible for use in collision calculations as too much computational time is required for generation of the Hamiltonian matrices. Therefore, we attempted to include important correlation effects for the target states and kept the CI expansions to a reasonable size by omitting all the insignificant configurations. In order to achieve this objective we first analyzed the full LS configuration expansions of Ti II, where we included the relativistic shift due to the mass correction and Darwin term without the spin–orbit interaction, which leads to the fine-structure splitting. The Ti II wave functions can be represented as a three electron system above the $3s^2 3p^6$ closed inner core. Our expansions contained all one- and two-valence electrons excitations to the spectroscopic and correlated orbitals described above. The resulting CI expansions accounted for the major valence–valence correlation effects. Then we considered one- and two-electron promotions of the inner core $3s$ and $3p$ orbitals to the valence orbitals to account for the single and double core–valence correlation effects. Both valence–valence correlation and core–valence correlation effects have been found to be important to obtain well-converged target wave functions. To keep the target CI expansions to a reasonable size, the final target expansions have been restricted to configurations with mixing coefficients equal to or larger than ∼0.02. Different terms of a configuration exhibit different convergence patterns and, therefore, required different cut-off parameters. Therefore, the final cut-off parameters have been varied in the range from 0.015 to 0.030 for the different terms. This cut-off scheme kept the resulting CI expansions of size from 300 to 600 for each LS target state. These CI expansions have been found manageable for the scattering calculation with the available modern computational resources. We then applied fine-tuning to the theoretical LS energies to bring them closer to the experimental weighted average over the fine-structure levels obtained from the NIST compilation (Kramida et al. 2015). We have been able to reach an agreement with observed LS energies of better than 0.1 eV for all considered states first by including all the significant configurations in the CI expansions and then by applying small corrections to the diagonal elements of the Hamiltonian matrices.

The Breit–Pauli Hamiltonian formed on the basis of multiconfiguration LS wave functions has been diagonalized to obtain J-dependent fine-structure levels energies. We used the CI approach with non-orthogonal orbitals (Zatsarinny & Froese Fisher 2000, 2009) in our calculations. The target CI expansions for fine-structure levels with the total angular momentum J and parity π are described as follows

$$\Psi^{\beta J\pi} = \sum_{\alpha LS} C(\beta J\pi;\ \alpha LS\pi)\Phi^{\alpha LS\pi}. \quad (1)$$

We included all three one-electron Breit–Pauli operators in our calculations of J-dependent target wave functions. We did not apply any cut-off parameter to the target CI expansions for the fine-structure levels. The target CI expansions for each total angular momentum J and parity π fine-structure level contain on an average 1000 configurations. These CI expansions have been found to be of manageable size in the subsequent collision calculation. In Equation (1), the functions $\Phi^{\alpha LS\pi}$ represent the multiconfigurational expansions from LS calculations and the coefficients $C(\beta J\pi;\ \alpha LS\pi)$ describe the spin–orbit mixing of different LS terms. The accuracy of transitions between the fine-structure levels depends significantly on the term mixing, which in turn depends on both the spin–orbit interaction and the energy separation between the LS states. The term mixing was improved by making additional fine-tuning of the calculated energies of fine-structure (LSJ) levels to closely agree with the observed energy levels. The purpose of the fine-tuning process is not only to bring the calculated energies closer to the measured values, but also to improve the mixing between levels. The fine-tuning procedure is frequently used in the structure calculations (Hibbert 1996). The forbidden transitions between the fine-structure levels are especially very sensitive to the mixing coefficients, and the fine-tuning procedure is found to improve significantly the accuracy of relatively weaker forbidden transitions.

2.2. Details of Collision Calculation

The electron-impact collision strengths for fine-structure excitation of Ti II have been calculated using an extended version of the BSR code (Zatsarinny 2006), which is based on the R-matrix method and employs B-splines as a basis for the continuum orbitals. The details of collision calculation can be found in our recent work for the electron-impact excitation of Fe II (Tayal & Zatsarinny 2018). Here we describe only the different steps of collision calculations that are specific to the present fine-structure excitation of Ti II. We first carried out calculation of the Hamiltonian matrices in LS-coupling and then these have been transformed to the intermediate coupling by adding the spin–orbit interaction for the scattering electron to the final Hamiltonian matrices. This approach provides the same level of accuracy as the direct Breit–Pauli calculation, and at the same time avoids repetition of calculations of non-relativistic Hamiltonian matrix elements for different J-values. The non-relativistic Hamiltonian matrices in the inner region for the close-coupling equation included 130 LS states and the scattering problem contained up to 402 scattering channels in the LS-coupling scheme. The partial waves up to $L = 50$ and total spin $S = 0$–2 have been considered giving rise to overall 306 partial waves. We chose an internal region of radius $a = 25\, a_0$ and the continuum orbitals have been represented by

96 B-splines of order 8 leading to the Hamiltonian matrices of size up to 40,000. A very large number of two-electron matrix elements have been involved in the construction of Hamiltonian matrices. The major computational effort was needed to calculate the huge number of overlap integrals due to the non-orthogonal term-dependent orbitals employed in the present calculation for different Ti II ionic states.

The Breit–Pauli matrices have been then constructed in several different steps using the transformation of LS Hamiltonian matrices to the intermediate-coupling scheme. First, we modified the LS Hamiltonian matrices using the fine-tuning of LS term energies discussed above. It simply requires modification of the diagonal matrix elements for the orthogonal one-electron orbitals, but for non-orthogonal orbitals the modification needed the diagonalization of the overlap matrices as discussed in our recent calculations for Fe II (Tayal & Zatsarinny 2018) in detail. Next, the Hamiltonian matrices in the internal region are transformed to the *jK* coupling scheme using the angular-coupling transformation coefficients. The term-coupling coefficients from Equation (1) have been used to transform Hamiltonian matrices from the *jK* coupling to full intermediate coupling utilizing a newly developed BSR_RECOUP computer program. Finally, the Hamiltonian matrices have been augmented with the spin–orbit interaction term for the scattering electron. This approach has two distinct advantages over the direct Breit–Pauli calculation; it allows us to apply fine-tuning to the energy of the LS terms and to include a much bigger scattering model than possible in the direct Breit–Pauli calculation. The fine-tuning is expected to improve the description of the target spin–orbit mixing, and consequently, it also improves the description of spin-forbidden transitions between fine-structure levels.

We included 314 fine-structure levels of Ti II $3d^24s$, $3d^3$, $3d4s^2$, $3d^24p$, $3d^25s$, $3d4s4p$, $3d^24d$, $3d^25p$, and $3d^24f$ configurations in our intermediate-coupling scattering model, indicated as BSR-314 in the following discussion. The B-spline R-matrix calculations have been performed for the lower 50 partial waves of total angular momentum up to $J = 24$ of both even and odd parities. The maximum number of channels in a single partial wave were 2050, and Hamiltonian matrices of size up to 200,000 were constructed. The parallel version of the STGF program (Ballance & Griffin 2004) was utilized in the outer region of the R-matrix box to calculate collision strengths. We used a fine energy grid of 10^{-4} Ry to adequately include resonance structures in collision strengths in the resonance energy region below the highest excitation threshold. However, an electron energy grid of 10^{-2} Ry was chosen for energies above the highest excitation threshold where the collision strengths exhibit a smooth variation with incident electron energies. The collision strengths have been calculated for 11,700 incident electron energies up to 10 Ry. The collision strengths for the forbidden, intercombination, and dipole-allowed transitions display different energy dependence, and have been extrapolated to higher energies above 10 Ry using the standard asymptotic energy dependence for the different types of transitions. The 50 partial waves are not sufficient, especially for the dipole-allowed transitions and for transitions between closely lying levels at higher electron energies. The contributions of higher partial waves have been estimated with a top-up procedure based on the Coulomb–Bethe method or on geometric series approximation to achieve partial wave convergence at all energies for different types of transitions.

The thermally averaged collision strengths $\Upsilon(T_e)$ have been calculated by convoluting the collision strengths Ω over a Maxwellian distribution for electron temperatures from 10^3 to 10^5 K as follows

$$\Upsilon_{i-j}(T_e) = \int_{E_{th}}^{\infty} dE\ \Omega_{i-j}(E) \exp -\left(\frac{E - E_{th}}{kT_e}\right). \quad (2)$$

Here T_e is the electron temperature, k is the Boltzmann constant, and E_{th} is the transition energy for the $i - j$ transition.

3. Results and Discussion

3.1. Excitation Energies and Transition Probabilities

In Table 1 we have displayed the present fine-tuned excitation energies and lifetimes for the first 98 fine-structure levels of Ti II, and compared present energies with the experimental values taken from the NIST compilation (Kramida et al. 2015). The excitation energies of all 314 fine-structure levels together with their lifetimes are given in the Supplementary Material. The levels in the table are arranged according to the energy positions of their LS terms and each level is assigned an index. The different transitions in the following discussion have been denoted by these indices. The fine-tuned excitation energies from the present calculation show excellent agreement with experimental values. The differences between the present fine-tuned and compiled results are within a few meV for most excitation energy levels. The previous calculations of Bautista et al. (2006) and Deb et al. (2009) as well as the present calculation used different fine-tuning procedures to bring ab initio calculated energies closer to experimental values. The fine-tuning procedure works very well only for cases where differences between the calculated ab initio energies and experimental energies are very small. Bautista et al. (2006) reported both ab initio and fine-tuned energies for the LS terms only, and reported an overall agreement of about 10% between their calculated ab initio energies and weighted experimental values for many terms. However, they also noted "uncomfortably large" differences for some even parity terms, especially for the a^2D term that could not be fine-tuned well because of strong mixing with other even parity terms. Deb et al. (2009) reported fine-tuned excitation energies for the 36 even parity fine-structure levels and obtained excellent agreement with measured values for the 30 excitation levels. They also could not fine tune the excitation energies of six $3d^3b^2D_{3/2,5/2}$, $d^2D_{3/2,5/2}$, and $3d^2(^3P)4sb^2P_{1/2,3/2}$ levels very well due to strong mixing between these levels. However, we have been able to fine tune excitation energies closer to the experimental values even for cases of strong mixing because of the use of flexible term-dependent non-orthogonal orbitals as well as due to the inclusion of all carefully chosen strong CI effects. Overall, our procedure of generating target wave functions should also lead to a better description of the spin–orbit term mixing.

In Table 2 we have presented our calculated results for the line strengths, oscillator strengths, and transition probabilities for the electric dipole-allowed and forbidden transitions between the 314 levels of Ti II. The radiative transition probabilities for both the dipole-allowed and dipole-forbidden transitions have been used for the calculations of lifetimes of excited levels. These lifetimes have been included in Table 1. There are a number of even-parity metastable levels that can decay to lower levels only via forbidden electric quadrupole (E2) and magnetic dipole (M1) transitions. The most extensive

Table 1
Ti II Fine-structure Levels Excitation Energies (in eV) and Lifetimes (in sec) Included in the Present Collision Calculations

Index	Configuration	Term	J	Present	NIST	$\tau(sec)$	Index	Configuration	Term	J	Present	NIST	$\tau(sec)$
1	$3d^2(^3F)4s$	a^4F	3/2	0.00000	0.00000		50	$3d^2(^3F)4p$	z^4D	1/2	4.02896	4.03350	3.17E-09
2			5/2	0.01160	0.01167	2.82E+04	51			3/2	4.03887	4.04221	3.20E-09
3			7/2	0.02790	0.02798	1.01E+04	52			5/2	4.05334	4.05405	3.24E-09
4			9/2	0.04891	0.04878	7.59E+03	53			7/2	4.06701	4.06261	3.19E-09
5	$3d^3$	b^4F	3/2	0.11420	0.11257	5.02E+05	54	$3d^2(^3F)4p$	z^2G	7/2	4.28070	4.28283	3.96E-09
6			5/2	0.12246	0.12199	5.95E+04	55			9/2	4.31027	4.30827	3.96E-09
7			7/2	0.13383	0.13481	2.57E+04	56	$3d^2(^3P)4p$	z^2S	1/2	4.64074	4.64081	4.59E-09
8			9/2	0.14812	0.15074	2.18E+04	57	$3d^2(^1D)4p$	z^2P	3/2	4.87525	4.86432	4.49E-09
9	$3d^2(^3F)4s$	a^2F	5/2	0.57452	0.57388	4.79E+02	60			1/2	4.90638	4.91904	5.86E-09
10			7/2	0.60657	0.60724	4.38E+02	58	$3d^2(^1D)4p$	y^2D	5/2	4.90302	4.89451	4.37E-09
11	$3d^2(^1D)4s$	a^2D	3/2	1.07937	1.07997	8.17E+01	59			3/2	4.90314	4.91013	3.49E-09
12			5/2	1.08996	1.08416	9.85E+01	61	$3d^2(^1D)4p$	y^2F	5/2	4.95328	4.95029	3.47E-09
13	$3d^3$	a^2G	7/2	1.11660	1.11558	1.65E+02	63			7/2	4.96524	4.96863	2.91E-09
14			9/2	1.12823	1.13052	1.13E+02	62	$3d^2(^3P)4p$	z^4S	3/2	4.96300	4.96274	3.35E-09
15	$3d^3$	a^4P	1/2	1.16012	1.16096	1.65E+01	64	$3d^2(^3P)4p$	y^4D	1/2	5.00436	5.00032	3.65E-09
16			3/2	1.16664	1.16493	1.68E+01	65			3/2	5.01417	5.01215	3.64E-09
17			5/2	1.18080	1.18010	1.67E+01	66			5/2	5.03061	5.03148	3.61E-09
18	$3d^3$	a^2P	1/2	1.21348	1.22137	4.07E+01	67			7/2	5.05413	5.05836	3.56E-09
19			3/2	1.22182	1.23687	1.67E+01	68	$3d^2(^3P)4p$	z^4P	1/2	5.20805	5.20693	3.96E-09
20	$3d^2(^3P)4s$	b^4P	1/2	1.23393	1.22408	8.85E+00	69			3/2	5.21614	5.21587	3.95E-09
22			3/2	1.24531	1.23126	8.30E+00	70			5/2	5.23125	5.23323	3.94E-09
21			5/2	1.24165	1.24292	1.36E+01	71	$3d^2(^1G)4p$	y^2G	7/2	5.42368	5.42316	2.98E-09
23	$3d^3$	b^2D	3/2	1.56805	1.56578	2.35E+01	72			9/2	5.42742	5.42815	2.97E-09
25			5/2	1.57971	1.58182	2.59E+01	73	$3d^2(^3P)4p$	x^2D	5/2	5.56699	5.56719	3.69E-09
24	$3d^3$	a^2H	9/2	1.57159	1.57176	2.64E+01	74			3/2	5.56477	5.56873	3.68E-09
26			11/2	1.58502	1.58388	2.95E+01	75	$3d^2(^3P)4p$	y^2P	1/2	5.63674	5.63787	4.13E-09
27	$3d^2(^1G)4s$	b^2G	7/2	1.89184	1.89170	6.13E+01	76			3/2	5.64824	5.64735	4.16E-09
28			9/2	1.89205	1.89271	5.79E+01	77	$3d^2(^1G)4p$	z^2H	9/2	5.66932	5.66282	3.94E-09
29	$3d^2(^3P)4s$	b^2P	1/2	2.04724	2.04772	7.40E+00	78			11/2	5.68713	5.69195	3.89E-09
30			3/2	2.06019	2.06127	7.26E+00	79	$3d^2(^1G)4p$	x^2F	7/2	5.88865	5.88513	4.45E-09
31	$3d^3$	b^2F	7/2	2.59189	2.59025	2.17E+00	80			5/2	5.90111	5.90475	4.42E-09
32			5/2	2.59610	2.59769	2.13E+00	81	$3d4s(^3D)4p$	^4F	3/2	6.49134	6.48808	5.17E-09
33	$3d4s^2$	c^2D	3/2	3.09369	3.09479	3.64E-01	84			5/2	6.50912	6.50569	2.27E-09
34			5/2	3.12440	3.12353	3.87E-01	86			7/2	6.53712	6.53462	2.53E-09
35	$3d^2(^3F)4p$	z^4G	5/2	3.66743	3.66305	4.86E-09	88			9/2	6.57409	6.58313	4.36E-09
36			7/2	3.68828	3.68662	4.82E-09	82	$3d4s(^3D)4p$	^4D	1/2	6.49376	6.48924	2.80E-09
37			9/2	3.71416	3.71560	4.78E-09	83			3/2	6.50514	6.50414	4.16E-09
38			11/2	3.74469	3.74940	4.73E-09	85			5/2	6.52313	6.52540	2.87E-09
39	$3d^2(^3F)4p$	z^4F	3/2	3.82408	3.82323	3.35E-09	87			7/2	6.54739	6.55221	6.75E-09
40			5/2	3.83700	3.83838	3.38E-09	89	$3d4s(^1D)4p$	w^2D	5/2	6.63947	6.63997	3.77E-09
41			7/2	3.85551	3.85760	3.35E-09	90			3/2	6.64568	6.64521	3.80E-09
43			9/2	3.87973	3.88084	5.73E-09	91	$3d4s(^3D)4p$	y^4P	1/2	6.96753	6.97079	3.88E-09
42	$3d^2(^3F)4p$	z^2F	5/2	3.86868	3.86924	3.30E-09	92			3/2	6.97329	6.97402	3.87E-09
44			7/2	3.90474	3.90438	5.70E-09	93			5/2	6.98680	6.98355	3.84E-09
45	$3d^2(^3F)4p$	z^2D	3/2	3.93664	3.93732	5.83E-09	95	$3d4s(^1D)4p$	w^2F	5/2	7.35836	7.35501	7.08E-09
47			5/2	3.97105	3.97067	2.91E-01	96			7/2	7.36956	7.37314	3.09E-09
46	$3d^24s$	a^2S	1/2	3.94105	3.94120	5.72E-09	94	$3d4s(^1D)4p$	^2P	3/2	7.35573	7.36317	3.06E-09
48	$3d^3$	d^2D	3/2	3.99879	4.00165	1.07E-02	97			1/2	7.37703	7.36964	7.33E-09
49			5/2	4.01187	4.00877	1.41E-02	98	$3d^2(^3F)5s$	e^4F	3/2	7.71038	7.70939	2.99E-09

(This table is available in its entirety in machine-readable form.)

calculation of radiative transition probabilities and lifetimes for the metastable levels of Ti II has been presented by Deb et al. (2009). Comparison of their lifetimes with the present results is given in Table 3. We note a very reasonable agreement between the two calculations with standard deviation of about 20%. However, there are a few levels with considerable disagreement. For example, the lifetimes of the $3d^32P_{1/2,3/2}$ levels of Deb et al. (2009) exceed our values by five times. For the $3d^32P$ state we found extremely strong, almost half and half, mixing with the $3d^24s^2P$ state. It makes even the configuration assignment for these levels somewhat ambiguous. The matrix elements for the levels with such strong mixing are very sensitive to the details of calculation and it may be the reason for a large disagreement with the CIV3 calculation in this case. Another example of large discrepancies is the levels $3d4s^22D_{3/2,5/2}$ which also show strong mixing

Table 2
Present Calculated Line Strengths (S), Oscillator Strengths (f_{ik}), and Transition Probabilities ($A_{ki}(s^{-1})$) for E1, E2, and M1 Transitions in Ti II Together with Their Wavelengths $\lambda(\AA)$

i	k	Type	$\lambda(\AA)$	S	f_{ik}	$A_{ki}(s^{-1})$
1	2	E2	1069071.97	1.03E+00	3.53E-17	1.37E-13
1	2	M1	1069071.97	9.64E+00	9.12E-09	3.55E-05
1	3	E2	444308.61	1.39E-01	6.63E-17	1.12E-12
1	5	M1	108568.07	3.06E-08	2.85E-16	1.61E-10
1	5	E2	108568.07	2.97E+01	9.75E-13	5.52E-07
1	6	E2	101241.75	2.87E+01	1.16E-12	5.03E-07
1	6	M1	101241.75	2.79E-04	2.78E-12	1.21E-06
1	7	E2	92643.34	3.54E+00	1.87E-13	7.26E-08
1	9	E2	21580.54	2.36E-06	9.84E-18	9.39E-11
1	9	M1	21580.54	3.39E-03	1.59E-10	1.52E-03
1	35	E1	3380.72	1.76E+01	3.95E-01	1.54E+08
1	39	E1	3242.23	1.38E+01	3.22E-01	2.04E+08
1	40	E1	3231.31	3.84E+00	9.03E-02	3.85E+07
1	45	E1	3149.53	4.62E-01	1.11E-02	7.49E+06
1	47	E1	3122.24	3.52E-02	8.56E-04	3.91E+05
1	50	E1	3077.36	5.30E+00	1.31E-01	1.84E+08
1	51	E1	3069.80	2.00E+00	4.95E-02	3.50E+07
1	52	E1	3058.85	1.35E-01	3.35E-03	1.59E+06

(This table is available in its entirety in machine-readable form.)

with the $3d^3$ configuration levels. In this case, the lifetimes from the CIV3 calculation are two times smaller than our values.

The comparison of the present calculated lifetimes with the measurements of Hartman et al. (2003, 2005) and Palmeri et al. (2008) has been presented in Table 3 for seven levels belonging to the $3d^3$, $3d^24s$, and $3d4s^2$ configurations. We have also included available theoretical results of Bautista et al. (2006) and Deb et al. (2009) in Table 3. Our calculated lifetimes closely agree with the measurement of Palmeri et al. within the experimental uncertainties. However, the differences with the measurements of Hartman et al. (2003) are up to a factor of 2. It indicates the importance of correction due to the repopulation effects that was incorporated in the measurement of Palmeri et al. (2008). It may also be the reason of discrepancies between the previous theoretical results of Deb et al. (2009) and Bautista et al. (2006) and experimental results of Hartman et al. (2003, 2005). Good agreement of the present results with measured lifetimes of Palmeri et al. (2008) confirms that our target wave function expansions adequately include main correlation corrections and also correctly reproduce the spin–orbit mixing.

The electric-dipole (E1) transitions in Ti II received much more attention both from experiment and theory. Lifetimes for selected higher-lying levels of Ti II, which decay through the E1 transitions, are given in Table 4. Comparison is made with the two most extended recent calculations of Kurucz (2011) and Ruczkowski et al. (2016), along with the available experimental data of Kwiatkowski et al. (1985), Bizzarri et al. (1993), Langhans et al. (1995), and Lundberg et al. (2016). Kurucz (2011) used a semi-empirical approach based on a superposition of configurations using a modified version of the Cowan (1981) codes and experimental level energies. We note a very good agreement of our lifetimes with the results of Kurucz (2011), with average deviation of 10%. Less satisfactory agreement is observed with the lifetimes reported by Ruczkowski et al. (2016), who used a semi-empirical oscillator strength parameterization method. The average deviation with their calculated results is 21.5%. The larger differences, up to a factor of 2, were found for the higher-lying $3d^25s$ levels. The agreement between our results and the experimental values is mostly within the experimental uncertainties. We note a good agreement between the present results and the most recent measurements of Lundberg et al. (2016) who have included the higher-lying $3d^25s$ levels. The new measured results are somewhat smaller than the previous measurements. The average deviation of the present calculated results with the measured lifetimes of Lundberg et al. (2016) is estimated to be within 5%.

The comparison of our calculated lifetimes for excited levels and radiative rates for dipole-allowed and forbidden transitions with the available experimental and other theoretical results to some extent indicates the accuracy of present target wave functions used in collision calculation. We have found a good agreement for the strong dipole-allowed E1 transitions as well as for the weak M1 and E2 forbidden transitions in Ti II. In order to illustrate the level of agreement between the present oscillator strengths and the existing radiative data sets for the individual E1 transitions, Figure 1 provides comparison between the present oscillator strengths (log gf) with the most recent other calculated results of Lundberg et al. (2016) who used the relativistic Hartree–Fock computer code of Cowan (1981). They also used a model potential to include core-polarization effects and applied a correction to the dipole operator in their calculations of radiative rates. The semi-empirically adjusted parameters yielded theoretical energy levels that have been noted to be very close to the experimental values. The calculation of Lundberg et al. (2016) for radiative rates represents one of the most comprehensive data for the dipole-allowed transitions in Ti II. The comparison in Figure 1 shows a reasonable agreement between the present results and the calculation of Lundberg et al. (2016), with average deviation of 30.5%. A better agreement is observed for the stronger transitions, where the agreement between the two sets of results is in the range of 10%–20%. The oscillator strengths for weaker transitions (typically log gf <-2) are extremely sensitive to small changes in the atomic wave functions, and the strong cancellation effects can lead to errors in the radiative rates ranging from 50% to a few orders of magnitude. Lundberg et al. (2016) found similar agreement with other previously available extensive semi-empirical calculations of Ruczkowski et al. (2016) and to some extent with that of Kurucz (2011). It may be noted that Kurucz (2011) and Lundberg et al. (2016) used very similar methods of calculation, except that the former did not include the core-polarization in his calculation. In Figure 2 we have displayed the comparison of the present oscillator strengths (log gf) with the experimental values reported by Lundberg et al. (2016) for 57 dipole-allowed transitions from the $5s$ levels. There is a very good agreement between our calculated results and the experimental values, with average deviation of 10.1 %. Lundberg et al. (2016) noted a good agreement between their experimental values and the previous Fourier Transform Spectroscopy measurements of Pickering et al. (2001) and Wood et al. (2013). It is worth noting that we have omitted configurations with smaller coefficients from our target CI expansions in order to keep them manageable in the subsequent scattering calculation. The accuracy of present radiative rates for weaker transitions can perhaps be further improved by

Table 3
Comparison of the Calculated and Experimental Lifetimes (ns) for the Metastable States in Ti II

				Theory			Experiment	
Index	Configuration	Term	J	This work	Bautista et al. (2006)	Deb et al. (2009)	Hartman et al. (2005)	Palmeri et al. (2008)
1	$3d^2(^3F)4s$	a^4F	3/2					
2			5/2	2.82E+04		2.77E+04		
3			7/2	1.01E+04		1.01E+04		
4			9/2	7.59E+03		7.83E+03		
5	$3d^3$	b^4F	3/2	1.14E+06		1.47E+06		
6			5/2	5.95E+04		5.08E+04		
7			7/2	2.57E+04		2.04E+04		
8			9/2	2.18E+04		1.72E+04		
9	$3d^2(^3F)4s$	a^2F	5/2	4.79E+02		3.20E+02		
10			7/2	4.38E+02		3.19E+02		
11	$3d^2(^1D)4s$	a^2D	3/2	8.17E+01		6.01E+01		
12			5/2	9.85E+01		7.08E+01		
13	$3d^3$	a^2G	7/2	1.65E+02		1.44E+02		
14			9/2	1.13E+02		9.30E+01		
15	$3d^2(^3P)4s$	a^4P	1/2	1.65E+01		1.26E+01		
16			3/2	1.68E+01		1.34E+01		
17			5/2	1.67E+01		1.30E+01		
18	$3d^3$	a^2P	1/2	4.07E+01		2.02E+02		
19			3/2	1.67E+01		1.05E+02		
20	$3d^3$	b^4P	1/2	8.85E+00		1.23E+01		
22			3/2	8.30E+00	3.11E+01	1.26E+01	1.80E+01(4)	
21			5/2	1.36E+01	1.64E+01	1.31E+01	2.80E+01(4)	1.60E+01(1)
23	$3d^3$	b^2D	3/2	2.35E+01		2.73E+01		
25			5/2	2.64E+01		3.33E+01		2.40E+01(3)
24	$3d^3$	a^2H	9/2	2.59E+01		3.37E+01		
26			11/2	2.95E+01		3.97E+01		
27	$3d^2(^1G)4s$	b^2G	7/2	6.13E+01		5.13E+01		
28			9/2	5.79E+01		5.69E+01		
29	$3d^2(^3P)4s$	b^2P	1/2	7.40E+00	1.27E+01	8.72E+00	1.40E+01(3)	7.70E+00(7)
30			3/2	7.26E+00		8.48E+00		7.00E+00(6)
31	$3d^3$	b^2F	7/2	2.17E+00		2.97E+00		
32			5/2	2.13E+00		2.95E+00		
33	$3d4s^2$	c^2D	3/2	3.64E-01	1.92E-01	1.80E-01	2.90E-01(1)	
34			5/2	3.87E-01	1.96E-01	1.90E-01	3.30E-01(2)	

setting much smaller cut-off parameters for generating configuration expansions, but it will lead to unmanageably large CI expansions for scattering calculation.

3.2. Collision Strengths for Fine-structure Excitation

We have calculated collision strengths for all fine-structure forbidden and allowed transitions between the 314 levels of Ti II. In Figure 3, we have displayed collision strengths as a function of incident electron energy for the two fine-structure forbidden $3d^24s^4F_{3/2} - {}^4F_{5/2}$ (1–2) and $3d^24s^4F_{3/2} - 3d^34F_{3/2}$ (1–5) transitions in the low-energy resonance region up to 0.6 Ry. It is clear from the figure that the collision strengths are dominated by the strong resonance structures, especially in the energy region from the lowest threshold at 0.00085 Ry to 0.30 Ry. There are several narrow and broad Rydberg series of resonances converging to various ionic thresholds. There are some strong and broad resonance features in the energy region from 0.1 to 0.2 Ry. The resonant collision strengths are several orders higher than the non-resonant collision strengths for the forbidden transitions. The temporary capture of the scattering electron to highly excited target states gives rise to various Rydberg series of resonances. These resonance structures at lower energies make a dominant contribution to the thermally averaged collision strengths at lower temperatures, and are very important for the accurate analysis and diagnostics of low-temperature astrophysical plasmas. The collision strengths of these transitions were also displayed by Bautista et al. (2006) in Figure 1 (a) and Figure 1 (d) of their publication. They also found similar resonance structures in their 82-level Breit–Pauli R-matrix calculation. Their collision strengths in the energy region below 0.3 Ry show good qualitative agreement with the present results. It may be noted that they have plotted $\log_{10}$ collision strengths in their paper, whereas we have displayed collision strengths as a function of the incident electron energy in Ry. It is important to correctly include overall contribution of the resonance structures to the convoluted effective collision strengths. The position and magnitude of resonance structures are likely to be more accurate in our calculation as we have used much better quality wave functions. There are some significant differences between the two calculations even for the background collision strengths for the forbidden $3d^24s^4F_{3/2} - {}^4F_{5/2}$ (1–2) transition. The two calculations differ approximately by 40% around 0.6 Ry, indicating significant differences in the quality of target wave functions used in scattering calculations.

In Figure 4, we have displayed collision strengths for the fine-structure dipole-allowed $3d^24s^4F_{3/2} - 3d^24p^4G_{5/2}$ (1–35)

Table 4
Comparison of the Experimental and Calculated Lifetimes (ns) for Ti II

			Theory				Experiment			
Index	Configuration	Term	Present	Kurucz (2011)	Ruczkowski et al. (2016)	Lundberg et al. (2016)	Kwiatkowski et al. (1985)	Bizzarri et al. (1993)	Langhans et al. (1995)	Lundberg et al. (2016)
35	$3d^2(^3F)4p$	$z^4G_{5/2}$	6.18	5.99	6.1		5.9(6)	5.7(3)		
36	$3d^2(^3F)4p$	$z^4G_{7/2}$	6.16	5.92	6.0		5.8(5)	5.6(3)		
37	$3d^2(^3F)4p$	$z^4G_{9/2}$	6.13	5.85	6.0		5.7(6)	5.6(3)		
38	$3d^2(^3F)4p$	$z^4G_{11/2}$	6.09	5.78	5.9		5.7(7)	5.6(3)		
39	$3d^2(^3F)4p$	$z^4F_{3/2}$	3.45	4.20	3.9		4.2(4)	4.1(2)	4.5(3)	
40	$3d^2(^3F)4p$	$z^4F_{5/2}$	3.48	4.15	3.8	3.76	4.1(3)	4.1(2)	4.3(3)	3.87(20)
41	$3d^2(^3F)4p$	$z^4F_{7/2}$	3.46	4.13	3.8		4.4(6)	4.1(2)	4.5(2)	
42	$3d^2(^3F)4p$	$z^2F_{5/2}$	5.53	7.09	7.2			6.8(3)		
43	$3d^2(^3F)4p$	$z^4F_{9/2}$	3.41	4.10	3.8		4.3(4)	4.1(2)	4.2(2)	
44	$3d^2(^3F)4p$	$z^2F_{7/2}$	5.50	6.99	7.1			6.8(3)		
45	$3d^2(^3F)4p$	$z^2D_{3/2}$	5.83	6.85	6.8	5.87	6.3(10)	6.6(3)		6.10(20)
47	$3d^2(^3F)4p$	$z^2D_{5/2}$	5.72	6.76	6.6		6.5(9)	6.6(3)		
50	$3d^2(^3F)4p$	$z^4D_{1/2}$	3.50	3.79	3.5		4.0(4)	3.9(2)	4.0(3)	
51	$3d^2(^3F)4p$	$z^4D_{3/2}$	3.53	3.85	3.6		4.1(5)	4.0(2)	4.0(3)	
52	$3d^2(^3F)4p$	$z^4D_{5/2}$	3.56	3.92	3.7	3.47	3.9(4)	4.0(2)	4.2(3)	3.86(20)
53	$3d^2(^3F)4p$	$z^4D_{7/2}$	3.51	3.85	3.6	3.40	4.1(5)	4.0(2)	4.2(3)	3.75(20)
54	$3d^2(^3F)4p$	$z^2G_{7/2}$	4.80	4.85	5.5			4.6(2)		
55	$3d^2(^3F)4p$	$z^2G_{9/2}$	4.79	4.85	5.5		4.8(4)	4.6(2)		
57	$3d^2(^1D)4p$	$z^2P_{3/2}$	4.57	4.46	5.1			5.5(3)		
58	$3d^2(^1D)4p$	$y^2D_{5/2}$	6.05	5.44	6.1			6.1(3)		
59	$3d^2(^1D)4p$	$y^2D_{3/2}$	4.48	5.50	4.2			4.5(2)		
60	$3d^2(^1D)4p$	$z^2P_{1/2}$	3.57	3.83	3.6			4.0(2)		
61	$3d^2(^1D)4p$	$y^2F_{5/2}$	3.99	4.43	3.7			3.9(2)		
62	$3d^2(^3P)4p$	$z^4S_{3/2}$	3.05	3.52	3.1			3.6(2)		
63	$3d^2(^1D)4p$	$y^2F_{7/2}$	3.89	3.76	3.5		4.1(4)	3.8(2)		
64	$3d^2(^3P)4p$	$y^4D_{1/2}$	4.27	4.48	3.3		4.6(5)	4.4(2)		
65	$3d^2(^3P)4p$	$y^4D_{3/2}$	4.27	4.46	3.3			4.5(2)		
66	$3d^2(^3P)4p$	$y^4D_{5/2}$	4.24	4.43	3.3		4.2(6)	4.3(2)		
67	$3d^2(^3P)4p$	$y^4D_{7/2}$	4.19	4.31	3.3			4.2(2)		
68	$3d^2(^3P)4p$	$z^4P_{1/2}$	4.38	4.81	4.6			4.8(2)		
69	$3d^2(^3P)4p$	$z^4P_{3/2}$	4.38	4.79	4.6			4.8(2)		
70	$3d^2(^3P)4p$	$z^4P_{5/2}$	4.37	4.76	4.6			4.8(2)		
71	$3d^2(^1G)4p$	$y^2G_{7/2}$	3.32	3.57	3.1			3.6(2)		
72	$3d^2(^1G)4p$	$y^2G_{9/2}$	3.31	3.57	3.1			3.7(2)		
73	$3d^2(^3P)4p$	$x^2D_{3/2}$	4.28	4.83	5.5			4.7(2)		
74	$3d^2(^3P)4p$	$x^2D_{5/2}$	4.27	4.81	5.5			4.7(2)		
75	$3d^2(^3P)4p$	$y^2P_{1/2}$	4.62	5.53	5.2			5.5(3)		
76	$3d^2(^3P)4p$	$y^2P_{3/2}$	4.65	5.53	5.3			5.5(3)		
77	$3d^2(^1G)4p$	$z^2H_{9/2}$	5.05	4.90	4.8			4.7(2)		
78	$3d^2(^1G)4p$	$z^2H_{11/2}$	5.01	4.81	4.7			4.6(2)		
79	$3d^2(^1G)4p$	$x^2F_{7/2}$	4.48	5.21	5.0			5.5(3)		
80	$3d^2(^1G)4p$	$x^2F_{5/2}$	4.47	5.16	5.0			5.4(3)		
98	$3d^2(^3F)5s$	$e^4F_{3/2}$	2.99	2.82	3.5	3.19				2.96(20)
99	$3d^2(^3F)5s$	$e^4F_{5/2}$	3.00	2.82		3.19				3.05(20)
100	$3d^2(^3F)5s$	$e^4F_{7/2}$	3.00	2.82	3.6	3.19				3.02(20)
101	$3d^2(^3F)5s$	$e^4F_{9/2}$	3.01	2.82		3.19				3.14(20)
102	$3d^2(^3F)5s$	$e^2F_{5/2}$	3.13	3.04	6.2	3.41				3.04(15)
105	$3d^2(^3F)5s$	$e^2F_{7/2}$	3.14	3.05	6.2	3.41				3.02(15)

and $3d^24s^4F_{3/2} - 3d^24p^4F_{3/2}$ (1-39) transitions as a function of incident electron energy in Ry. The collision strengths are shown from the lowest excitation threshold energy to 10 Ry to illustrate the energy behavior at higher energies. The collision strengths show characteristic energy behavior of the dipole-allowed transitions. The magnitude of collision strengths at higher electron energies is directly related to the oscillator strengths for the dipole-allowed transitions, which in turn depends up on the quality of target wave functions. The dipole-allowed $3d^24s^4F_{3/2} - 3d^24p^4G_{5/2}$ (1–35) and $3d^24s^4F_{3/2} - 3d^24p^4F_{3/2}$ (1–39) transitions are strong and give rise to intense ultraviolet features at 3380.72 and 3242.23 Å in astrophysical plasmas. The present oscillator strength (f-value) for the $3d^24s^4F_{3/2} - 3d^24p^4G_{5/2}$ (1–35) transition is 0.395 and compares very well (within 10%) with the measured values of 0.361 (Pickering et al. 2001) and 0.353 (Bizzarri et al. 1993) and the calculated result 0.396 of Kurucz (2000). However, the present result differs from the calculated value of 0.222 from Bautista et al. (2006) by

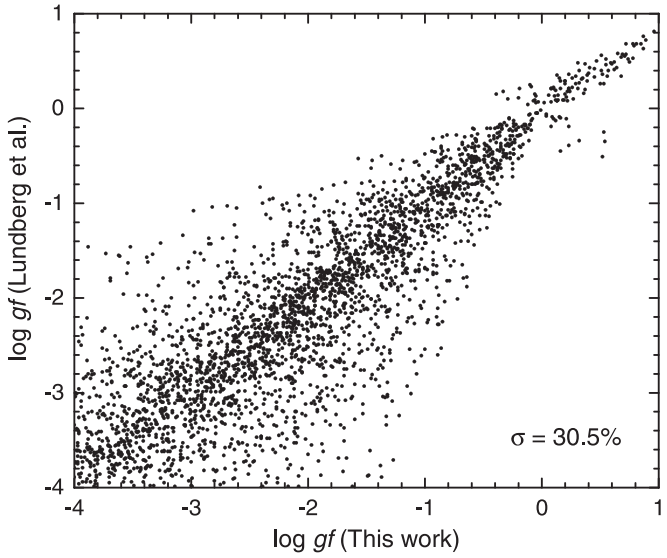

Figure 1. The log gf values from present calculation have been compared with the semi-empirical calculation of Lundberg et al. (2016) for allowed transitions from even parity levels to odd parity levels in Ti II. The average deviation between the two calculations has been indicated.

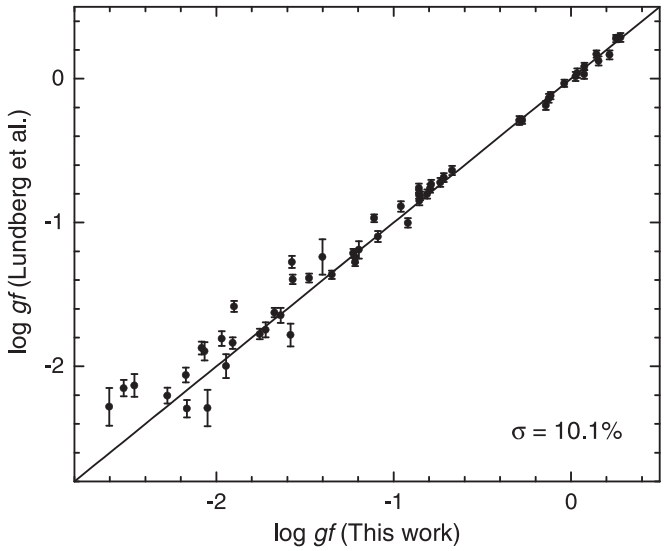

Figure 2. Comparison between the present calculated log gf and the measured values of Lundberg et al. (2016) for dipole-allowed transitions from the 5*s* levels. The average deviation between the calculation and experiment has been indicated.

about 44%. The $3d^24s^4F_{3/2} - 3d^24p^4F_{3/2}$ (1–39) transition has oscillator strength of 0.322 from the present calculation and 0.250 and 0.233 from the calculation of Kurucz (2000) and measurement of Pickering et al. (2001), respectively, where differences are about 25%. The behavior of collision strengths at higher energies can also provide a check on the convergence of the partial wave expansions. The dipole-allowed transitions are dominated by large angular momenta partial waves at higher incident electron energies. In the present work partial waves for the total angular momenta $J = 0$–24 have been calculated in the B-spline R-matrix calculations and the contributions of higher partial waves have been estimated in a top-up procedure to provide converged collision strengths. It is clear from Figure 4 that the resonance contribution to the excitation of the dipole-allowed transitions is very small, and the thermally averaged collision strengths basically depend on the background non-resonant collision strengths. There are a very few narrow resonances at low energies that are likely to make minor contributions to thermally averaged collision strengths. We have chosen these two strong dipole-allowed transitions, which demonstrate characteristic $ln(E)$ asymptotic behavior at higher energies.

Table 5 displays effective collision strengths $\Upsilon_{i-j}(T_e)$) obtained by convoluting collision strengths Ω with a Maxwellian electron energy distribution at temperatures from 1000 K to 100,000 K. The indices i and j represent lower and upper levels of a transition and have been assigned to levels in Table 1. The table of effective collision strengths for all transitions between the lowest 314 fine-structure levels of Ti II is available online in a machine-readable format with an associated ReadMe file. These transitions include many infrared, optical, and ultraviolet emission lines observed in low-density astrophysical plasmas, and should play an important role in their analysis and modeling. The only previously available calculation of Bautista et al. (2006) for electron excitation collision rates at temperatures between 5000 and 20,000 K of Ti II appears to be primarily performed for application in their modeling calculations. We note significant differences with their effective collision strengths for many dipole-allowed and forbidden transitions. Our prime objective in the present work is to provide detailed collision and radiative rates needed for reliable Ti abundance determination in a variety of astrophysical objects.

The present effective collision strengths for the forbidden fine-structure $3d^24s^4F_{3/2} - {}^4F_{5/2}$ (1–2), $3d^24s^4F_{3/2} - {}^4F_{7/2}$ (1–3), $3d^24s^4F_{3/2} - {}^4F_{9/2}$ (1–4), $3d^24s^4F_{3/2} - 3d^34F_{3/2}$ (1–5), $3d^24s^4F_{3/2} - 3d^34F_{5/2}$ (1–6), and $3d^24s^4F_{3/2} - 3d^34F_{7/2}$ (1–7) transitions have been compared with the 82-state Breit–Pauli R-matrix calculation (RM-82) in Figure 5. The effective collision strengths for transitions from the ground level to the first three excited levels of the ground $3d^24s$ configuration have been displayed in the upper panels. The lower panels of the figure display transitions from the ground level to the lowest three levels of the $3d^3$ configuration. It is clear from Figure 5 that there are significant discrepancies between the two calculations in magnitude as well as in the behavior of effective collision strengths with temperature. There is a reasonable agreement only for the lowest $3d^24s^4F_{3/2} - {}^4F_{5/2}$ (1–2) transition. The present results are larger than the calculation of Bautista et al. (2006) for all six transitions displayed in Figure 5. There are large differences at lower temperatures where resonance structures make substantial contributions to the effective collision strengths. The present calculation exhibits stronger resonance structures in the near-threshold energy region and larger background collision strengths than the RM-82 calculation. Another reason for the differences at lower temperatures may be due to the differences in excitation thresholds. The discrepancies at higher temperatures are primarily due to the differences in target wave functions.

The comparison between the present effective collision strengths and the calculation of Bautista et al. (2006) for the dipole-allowed transitions as a function of $\log_{10}$ T (electron temperature in K) is shown in Figure 6. We have chosen six dipole-allowed fine-structure $3d^24s^4F_{3/2} - 3d^2(^3F)4p^4G_{5/2}$ (1–35), $3d^24s^4F_{3/2} - 3d^2(^3F)4p^4F_{3/2}$ (1–39), $3d^24s^4F_{3/2} - 3d^2(^3F)4p^4D_{5/2}$ (1–51), $3d^34F_{3/2} - 3d^2(^3F)4p^4G_{5/2}$ (5–35),

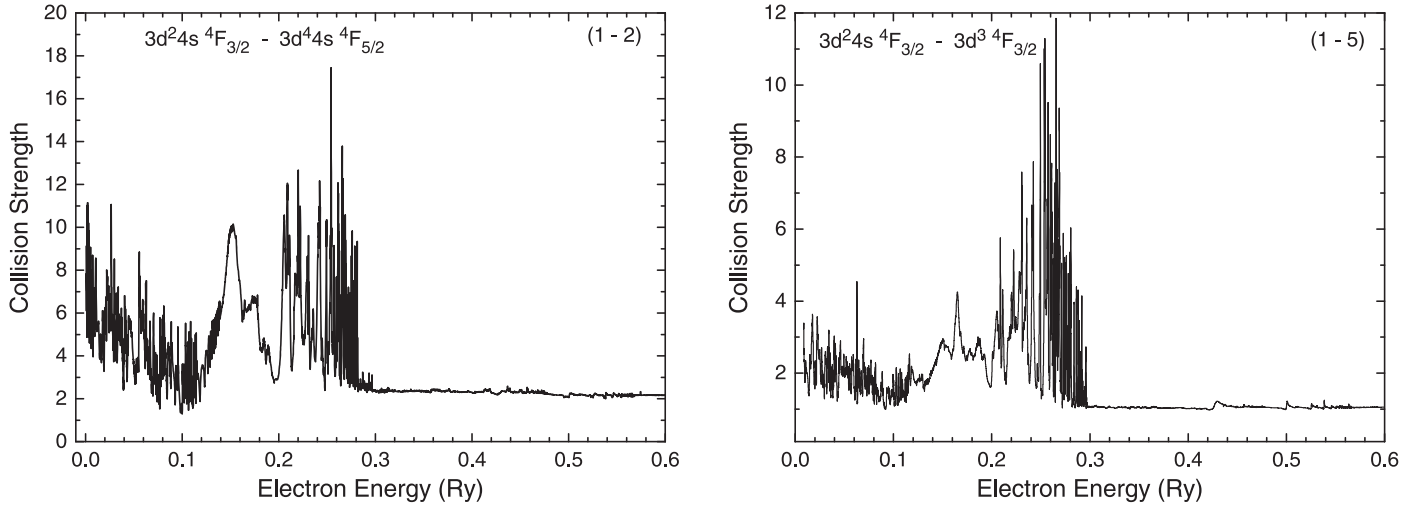

Figure 3. Collision strengths for the fine-structure forbidden $3d^24s^4F_{3/2} - {}^4F_{5/2}$ (1–2) and $3d^24s^4F_{3/2} - 3d^{34}F_{3/2}$ (1–5) transitions shown as a function of incident electron energy in Ry.

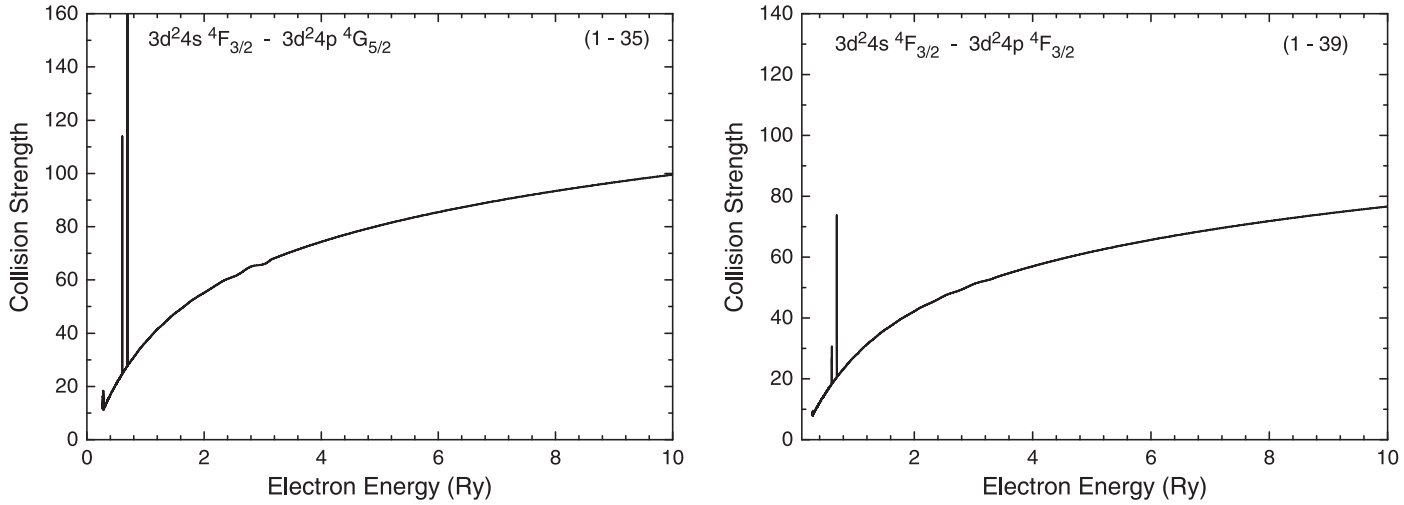

Figure 4. Collision strengths for the fine structure allowed $3d^24s^4F_{3/2} - 3d^24p^4G_{5/2}$ (1–35) and $3d^24s^4F_{3/2} - 3d^24p\_^4F_{3/2}$ (1–39) transitions plotted as a function of incident electron energy in Ry.

Table 5
Effective Collision Strengths for Electron-impact Excitation of Ti II

i	j	1000 K	1500 K	2000 K	2300 K	2500 K	5000 K	7500 K	10000 K	13000 K	15000 K	…
1	2	6.83E+00	6.49E+00	6.25E+00	6.14E+00	6.06E+00	5.46E+00	5.19E+00	5.05E+00	4.95E+00	4.89E+00	…
1	3	2.85E+00	2.66E+00	2.54E+00	2.48E+00	2.45E+00	2.18E+00	2.06E+00	2.01E+00	1.96E+00	1.94E+00	…
1	4	1.14E+00	1.03E+00	9.62E-01	9.34E-01	9.19E-01	8.10E-01	7.68E-01	7.49E-01	7.36E-01	7.27E-01	…
1	5	2.22E+00	2.23E+00	2.21E+00	2.20E+00	2.19E+00	2.10E+00	2.06E+00	2.06E+00	2.07E+00	2.08E+00	…
1	6	2.04E+00	2.04E+00	2.03E+00	2.02E+00	2.01E+00	1.86E+00	1.76E+00	1.69E+00	1.64E+00	1.60E+00	…
1	7	1.32E+00	1.30E+00	1.27E+00	1.25E+00	1.24E+00	1.10E+00	1.01E+00	9.56E-01	9.08E-01	8.82E-01	…
1	8	3.25E-01	3.48E-01	3.56E-01	3.56E-01	3.56E-01	3.26E-01	2.97E-01	2.76E-01	2.58E-01	2.48E-01	…
1	9	1.42E+00	1.46E+00	1.47E+00	1.46E+00	1.46E+00	1.46E+00	1.48E+00	1.49E+00	1.48E+00	1.47E+00	…
1	10	4.95E-01	5.27E-01	5.40E-01	5.42E-01	5.42E-01	5.14E-01	4.86E-01	4.64E-01	4.40E-01	4.26E-01	…
1	11	1.10E+00	1.05E+00	1.02E+00	1.00E+00	9.92E-01	9.33E-01	9.25E-01	9.27E-01	9.32E-01	9.35E-01	…
…	…	…	…	…	…	…	…	…	…	…	…	…

Note. i and j indicate the lower and upper levels indices, and the following columns indicate the electron temperature in K. The full table includes effective collision strengths at 18,000, 20,000, 30,000, 40,000, 50,000, 60,000, 70,000, 80,000, 90,000, and 1,00,000 K.

(This table is available in its entirety in machine-readable form.)

$3d^{34}F_{3/2} - 3d^2(^3F)4p^4F_{3/2}$ (5–39), and $3d^{34}F_{3/2} - 3d^2(^3P)4p^4D_{1/2}$ (5–50) transitions for comparison. These transitions are from the lower even parity $3d^24s^4F_{3/2}$ and $3d^{34}F_{3/2}$ levels to higher odd parity levels of the $3d^24p$ configuration. The resonance structures are expected to make only small contributions to the effective collision strengths in the

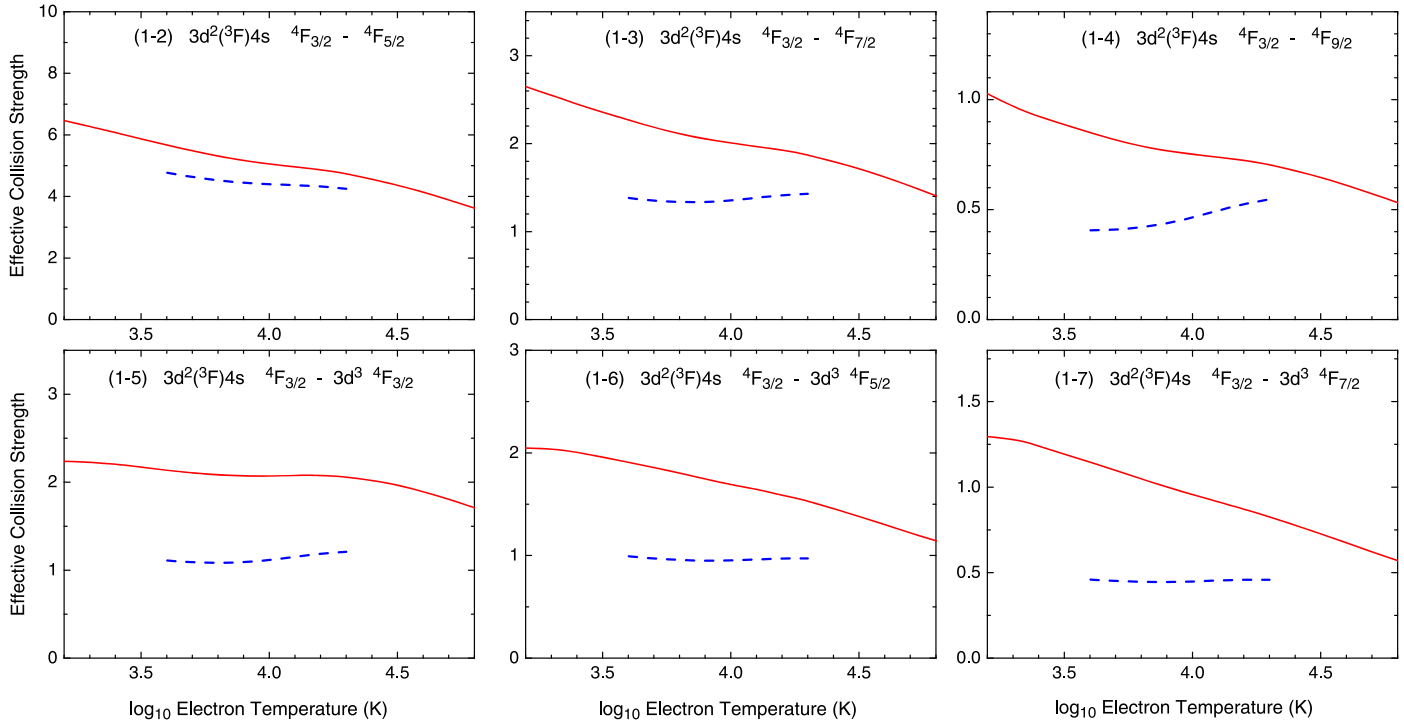

Figure 5. Effective collision strengths have been displayed as a function of $\log_{10}$ T (electron temperature in K) for the fine-structure forbidden $3d^24s^4F_{3/2} - {}^4F_{5/2}$ (1–2), $3d^24s^4F_{3/2} - {}^4F_{7/2}$ (1–3), $3d^24s^4F_{3/2} - {}^4F_{9/2}$ (1–4), $3d^24s^4F_{3/2} - 3d^{34}F_{3/2}$ (1–5), $3d^24s^4F_{3/2} - 3d^{34}F_{5/2}$ (1–6), and $3d^24s^4F_{3/2} - 3d^{34}F_{7/2}$ (1–7) transitions. The present RM-314 results (solid red line) have been compared with the RM-82 calculation of Bautista et al. (2006) (dashed blue line).

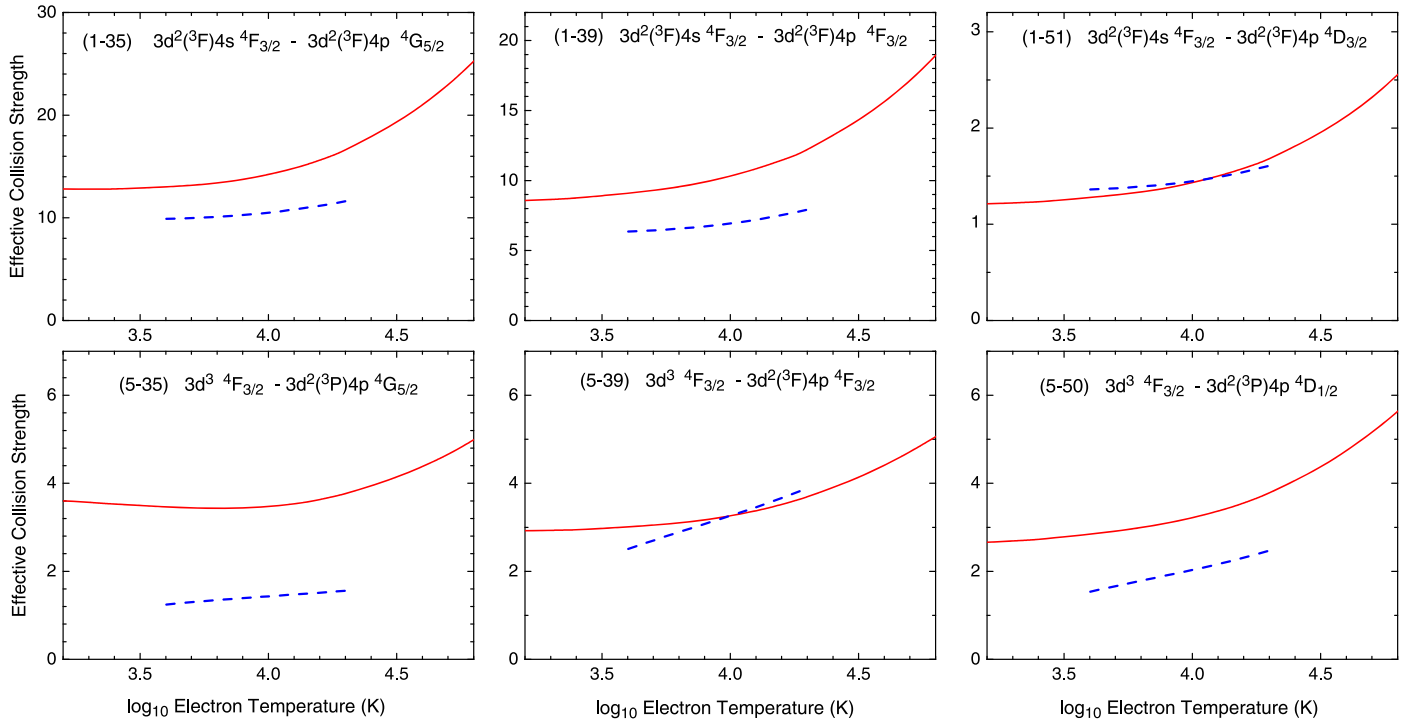

Figure 6. Effective collision strengths have been displayed as a function of $\log_{10}$ electron temperature in K for the fine-structure dipole-allowed $3d^24s^4F_{3/2} - 3d^2(^3F)4p^4G_{5/2}$ (1–35), $3d^24s^4F_{3/2} - 3d^2(^3F)4p^4F_{3/2}$ (1–39), $3d^24s^4F_{3/2} - 3d^2(^3F)4p^4D_{5/2}$ (1–51), $3d^{34}F_{3/2} - 3d^2(^3F)4p^4G_{5/2}$ (5–35), $3d^{34}F_{3/2} - 3d^2(^3F)4p^4F_{3/2}$ (5–39), and $3d^{34}F_{3/2} - 3d^2(^3P)4p^4D_{1/2}$ (5–50) transitions. The present RM-314 results (solid red line) have been compared with the RM-82 calculation of Bautista et al. (2006) (dashed blue line).

low-energy region for the dipole-allowed transitions. There is a mixed agreement of the present results with the calculation of Bautista et al. (2006). There is a good agreement of about 30% for the $3d^24s^4F_{3/2} - 3d^2(^3F)4p^4G_{5/2}$ (1–35), $3d^24s^4F_{3/2} - 3d^2(^3F)4p^4F_{3/2}$ (1–39), $3d^24s^4F_{3/2} - 3d^2(^3F)4p^4D_{5/2}$ (1–51), $3d^{34}F_{3/2} - 3d^2(^3F)4p^4F_{3/2}$ (5–39), and

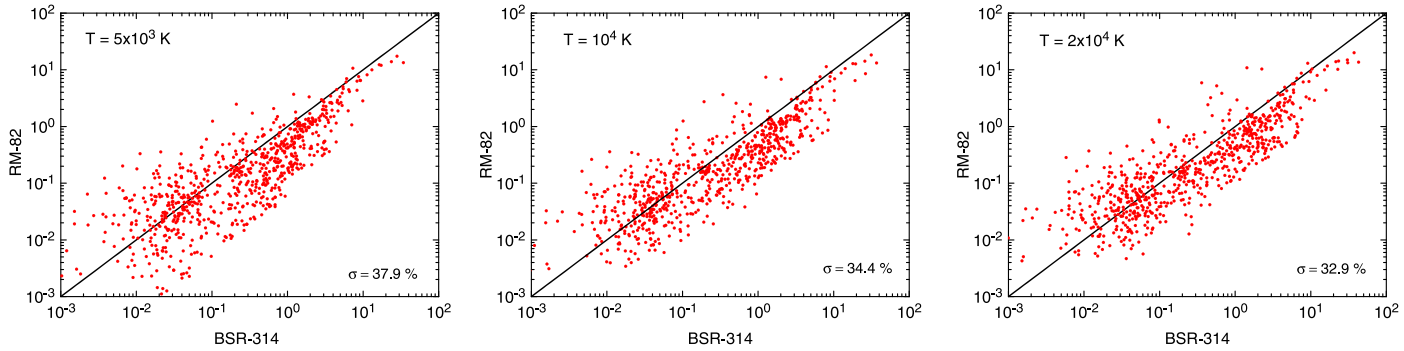

Figure 7. Present effective collision strengths for the fine-structure transitions between the lowest 12 levels have been compared with Bautista et al. (2006). The average deviations of RM-82 from the present BSR-314 are indicated in each panel.

$3d^34F_{3/2} - 3d^2(^3P)4p^4D_{1/2}$ (5–50) transitions. The large discrepancies are noted for the $3d^34F_{3/2} - 3d^2(^3F)4p^4G_{5/2}$ (5–35) transition where present results are larger by about a factor of two. The discrepancies between the two calculations are likely caused by the differences in target wave functions and, therefore, by the oscillator strengths. It is clear from the upper panels of Figure 6 that the dipole-allowed $3d^24s^4F_{3/2} - 3d^2(^3F)4p^4G_{5/2}$ (1–35), $3d^24s^4F_{3/2} - 3d^2(^3F)4p^4F_{3/2}$ (1–39) transitions are stronger with oscillator strengths 0.395 and 0.322, respectively, than the $3d^24s^4F_{3/2} - 3d^2(^3F)4p^4D_{5/2}$ (1–51) transition which has oscillator strength of 0.0495. The other three transitions in the lower panels have similar magnitudes. The effective collision strengths display characteristic behavior of the dipole transitions at higher temperatures.

The comparison between effective collision strengths from the BSR-314 and RM-82 calculations for all forbidden and allowed transitions between the lowest 12 levels of the $3d^2(^3F)4s$, $3d^3$, and $3d^2(^1D)4s$ configurations and from these levels to all other higher excitation levels considered by Bautista et al. (2006) has been shown in Figure 7 at 5000, 10,000, and 20,000 K electron temperatures. The agreement between the two calculations somewhat improves with increasing temperature. The average deviations at 5000 K, 10,000 K, and 20,000 K are 37.9%, 34.4%, and 32.9%, respectively. For some individual transitions we noted large discrepancies between the two calculations, which may have been caused by the differences in background collision strengths as well as by resonance structures in the low-energy region. In addition, we found substantial discrepancies with Bautista et al. (2006) for transitions between higher-lying excited levels, probably caused by errors in identification of levels in their calculation. The resonance structures in the energy region close to thresholds are more accurate in our calculations because of the inclusion of a larger number of levels in the close-coupling expansion. The background collision strengths in our calculation are expected to be of better accuracy due to better description of the target wave functions. Bautista et al. (2006) considered 5000–20,000 K temperature range, while we considered a much wider range of temperatures from 1000 K to 100,000 K. In the absence of the details of target wave functions and scattering calculation of Bautista et al. (2006), it is rather difficult to determine definitive reasons for significant discrepancies. The positions of resonances close to the threshold energy region are sensitive to the accuracy of target threshold energies and the convergence of the close-coupling expansions. Even though the present fine-tuned threshold energies agree with measured values to better than 0.01 eV for most levels and we have included a large number of levels in the close-coupling expansion, there is a possibility that the results may be somewhat less accurate at very low temperatures.

4. Summary

We have reported radiative transition rates and thermally averaged collision strengths for both forbidden and allowed transitions among the 314 fine-structure levels of Ti II belonging to terms of the ground $3d^24s$ and excited $3d^3$, $3d4s^2$, $3d^24p$, $3d^25s$, $3d4s4p$, $3d^24d$, $3d^25p$, and $3d^24f$ configurations. Overall, our data include 49142 transitions, and represent the first comprehensive data set for Ti II abundance determination in different astrophysical sources. The collision calculations have been performed using the B-spline Breit–Pauli R-matrix method. The B-splines are employed as a basis for the representation of continuum orbitals. The different modules of the BSR computer code have been modified in the last couple of years to deal with complicated iron-peak elements. The non-orthogonal orbitals have been generated both for the description of the target states as well as for the scattering continuum functions. The optimization of different atomic wave functions independently and well chosen important correlation configurations provided a very accurate description of the target states. The term-dependent one-electron orbitals also provided accurate representation of relaxation effects in configurations with different occupation in the $3d$ sub shell. Extensive valence–valence and core–valence correlation effects, relativistic effects, and term mixing are accounted for through the Breit–Pauli approximation. The accuracy of collision rates was further improved by using the fine-tuned target level energies. The fine-tuning process also enhanced the accuracy of the term-mixing coefficients for the target description used in our calculations of radiative and collision rates.

Based on the detailed comparison of radiative rates with the other calculations and available experimental results and limited comparison of collision rates with Bautista et al. (2006), our data should be accurate to about 30% or better for many transitions of astrophysical importance, but may be less accurate for weak transitions involving strong mixing and cancellation effects or for transitions between closely lying levels. The complete list of radiative data and effective collision strengths are presented in the supplementary materials for the abundance determination in astronomical objects.

The authors gratefully acknowledge Dr. Manuel Bautista for providing electronic effective collision strengths of Ti II from their R-matrix calculation. This work was supported by the United States National Science Foundation under grant Nos. AST-1714159 (*SST*) and OAC-1834740 (OZ). The numerical calculations were performed on STAMPEDE at the Texas Advanced Computing Center. They were made possible by the XSEDE allocations Nos. PHY-170047 and PHY-090031.

ORCID iDs

S. S. Tayal https://orcid.org/0000-0003-1805-0930

References

Ballance, C. P., & Griffin, D. C. 2004, JPhB, 37, 2943
Bautista, M. A., Hartman, H., Gull, T. R., et al. 2006, MNRAS, 370, 1991
Bizzarri, A., Huber, M. C. E., Noels, A., et al. 1993, A&A, 273, 707
Burke, P. G., Burke, V. M., & Dunseath, K. M. 1994, JPhB, 27, 5341
Cowan, R. D. 1981, The Theory of Atomic Structure and Spectra (Berkeley, CA: Univ. of California Press)
Deb, N. C., Hibbert, A., Felfli, Z., & Msezane, A. Z. 2009, JPhB, 42, 015701
Froese Fischer, C., Tachiev, G., Gaigalas, G., & Godefroid, M. R. 2007, CoPhC, 176, 559
Hartman, H., Rostohar, D., Derkatch, A., et al. 2003, JPhB, 36, L197
Hartman, H., Schef, P., Lundin, P., et al. 2005, MNRAS, 361, 206
Hibbert, A. 1975, CoPhC, 9, 141
Hibbert, A. 1996, PhST, T65, 104
Hibbert, A., Glass, R., & Fischer, C. F. 1991, CoPhC, 64, 455
Kramida, K., Ralchenko, Yu., Reader, J. & NIST ASD Team 2015, NIST Atomic Spectra Database (ver. 5.3) (Gaithersburg, MD: National Institute of Standards and Technology) [Online]. Available: http://physics.nist.gov/asd [2016, April 28]. National Institute of Standards and Technology, Gaithersburg, MD
Kurucz, R. L. 2000, Available at: http://cfaku5.harvard.edu/
Kurucz, R. L. 2011, Available at: http://kurucz.harvard.edu/atoms/2201/life2201.dat
Kwiatkowski, M., Werner, K., & Zimmermann, P. 1985, PhRvA, 31, 2695
Langhans, G., Schade, W., & Helbig, V. 1995, ZPhyD, 34, 151
Lundberg, H., Hartman, H., Engström, L., Nilsson, H., et al. 2016, MNRAS, 460, 356
Meyer, D. M., Lanzeta, K. M., & Wolfe, A. M. 1995, ApJL, 45, L13
Palmeri, P., Quinet, P., Biemont, E., et al. 2008, JPhB, 41, 125703
Pickering, J. C., Thorne, A. P., & Perez, R. 2001, ApJS, 132, 403
Prochaska, J., & Wolfe, A. M. 1999, ApJS, 121, 369
Royen, P., Gurell, J., Lundin, P., et al. 2007, PhRvA, 76, 030502
Ruczkowski, J., Elantkowska, M., & Dembczyński, J. 2016, JQSRT, 176, 6
Tayal, S. S., & Zatsarinny, O. 2018, PhRvA, 98, 012706
Tayal, S. S., & Zatsarinny, O. 2020, ApJ, 888, 10
Wiese, L. M., Fedchak, J. A., & Lawler, J. E. 2001, ApJ, 547, 1178
Wood, M. P., Lawler, J. E., Sneden, C., & Cowan, J. J. 2013, ApJL, 787, L16
Zatsarinny, O. 2006, CoPhC, 174, 273
Zatsarinny, O., & Froese Fisher, C. 2000, CoPhC, 12, 247
Zatsarinny, O., & Froese Fisher, C. 2009, CoPhC, 180, 2041